Commun. Comput. Phys.
doi: 10.4208/cicp.060710.040811s

Vol. **11**, No. 4, pp. 1236-1260
April 2012

Vlasov-Fokker-Planck Simulations for High-Power Laser-Plasma Interactions

Su-Ming Weng[1,3], Zheng-Ming Sheng[1,2,*], Hui Xu[4] and Jie Zhang[1,2]

[1] *Beijing National Laboratory of Condensed Matter Physics, Institute of Physics, CAS, Beijing 100190, China.*
[2] *Key Laboratory for Laser Plasmas (MoE) and Department of Physics, Shanghai Jiaotong University, Shanghai 200240, China.*
[3] *Theoretical Quantum Electronics (TQE), Technische Universität Darmstadt, D-64289 Darmstadt, Germany.*
[4] *Shandong Provincial Key Laboratory of Laser Polarization and Information Technology, Department of Physics, Qufu Normal University, Qufu 273165, China.*

Received 6 July 2010; Accepted (in revised version) 4 August 2011

Available online 29 November 2011

Abstract. A review is presented on our recent Vlasov-Fokker-Planck (VFP) simulation code development and applications for high-power laser-plasma interactions. Numerical schemes are described for solving the kinetic VFP equation with both electron-electron and electron-ion collisions in one-spatial and two-velocity (1D2V) coordinates. They are based on the positive and flux conservation method and the finite volume method, and these two methods can insure the particle number conservation. Our simulation code can deal with problems in high-power laser/beam-plasma interactions, where highly non-Maxwellian electron distribution functions usually develop and the widely-used perturbation theories with the weak anisotropy assumption of the electron distribution function are no longer in point. We present some new results on three typical problems: firstly the plasma current generation in strong direct current electric fields beyond Spitzer-Härm's transport theory, secondly the inverse bremsstrahlung absorption at high laser intensity beyond Langdon's theory, and thirdly the heat transport with steep temperature and/or density gradients in laser-produced plasma. Finally, numerical parameters, performance, the particle number conservation, and the energy conservation in these simulations are provided.

AMS subject classifications: 82D10, 82C31, 78M12, 80A20

Key words: Vlasov-Fokker-Planck equation, electric conductivity, inverse bremsstrahlung, nonlocal heat transport, positive and flux conservation method, finite volume method.

*Corresponding author. *Email addresses:* `Su-Ming.Weng@physik.tu-darmstadt.de` (S.-M. Weng), `zmsheng@sjtu.edu.cn` (Z.-M. Sheng)

1 Introduction

In the area of high-power laser-plasma interactions, non-Maxwellian electron distribution functions (EDFs) extensively exist in many important processes, such as the generation of plasma current under a strong direct current (DC) electric field, the inverse bremsstrahlung (IB) absorption in an intense laser field, and the nonlocal electron heat transport due to a steep temperature gradient. The well-known transport theory by Spitzer and Härm [1] can be used to calculate the generated plasma current as well as the electron heat flux, and Langdon's IB operator [2] can handle the IB absorption consistently with the evolution of EDF. However, these models are based on the linear perturbation theory with the weak anisotropy assumption of EDF. Therefore, Spitzer-Härm's theory is valid only under a weak DC electric field and a small temperature gradient, and Langdon's operator is valid only at a low laser intensity with a high plasma temperature. In order to describe the nonlinear processes with highly non-Maxwellian EDFs occurring in high-power laser-plasma interactions, a full solution of the kinetic equation such as the Vlasov-Fokker-Planck (VFP) equation without perturbation approximations is necessary.

In this paper, we apply our developed VFP simulation code to study plasma kinetics in a strong DC electric field, an intense laser field, or under a steep temperature gradient. In Section 2, we present the numerical scheme for solving the VFP equation with highly non-Maxwellian EDFs. We update the configuration space part of the VFP equation by the positive and flux conservation method [3, 4], and the velocity space part by the finite volume method [5], which extends the finite difference method [6]. Then we apply our simulation code to three typical problems with highly non-Maxwellian EDFs developed. We investigate the plasma current generation in a strong DC electric field in Section 3.1, the nonlinear IB absorption with a wide plasma temperature range at the high laser intensity in Section 3.2, and the nonlocal heat transport with a steep temperature gradient in Section 3.3. In Section 3.4, numerical parameters, performance, the particle number conservation, and the energy conservation are revealed. Finally, a summary is given in Section 4.

2 Vlasov-Fokker-Planck equation and numerical schemes

2.1 Master equation

In the kinetic theory, the plasma is usually described by the particle distribution functions $f^a(\mathbf{x},\mathbf{v},t)$, which can be considered as the possibility to find particle a in the 6-dimension phase space between $(\mathbf{x},\mathbf{v}) \to (\mathbf{x}+d\mathbf{x},\mathbf{v}+d\mathbf{v})$ at time t. Since most plasma properties are determined by electrons, we just consider the time evolution of the EDF in this paper. In an unmagnetized fully ionized plasma, the time evolution of the EDF can be described

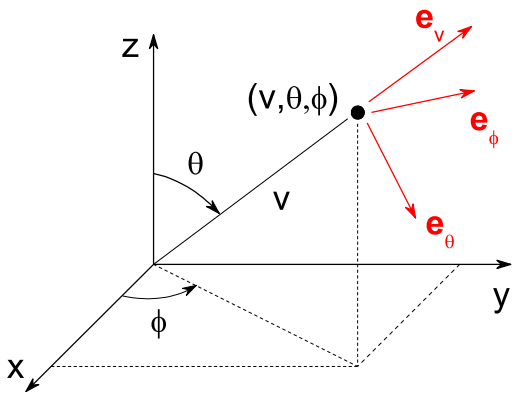

Figure 1: The spherical coordinate system in the velocity space, v is the magnitude of the velocity, θ is the polar angle between the zenith direction z and the velocity, ϕ is the azimuthal angle measured from the azimuth reference direction x to the orthogonal projection of the velocity on the reference $x-y$ plane, and $\mathbf{e}_v$, $\mathbf{e}_\theta$, $\mathbf{e}_\phi$ are the local orthogonal unit vectors at (v,θ,ϕ) in the directions of increasing v, θ, ϕ, respectively.

by the well-known Vlasov-Fokker-Planck equation

$$\frac{\partial f^e}{\partial t}+\mathbf{v}\cdot\nabla f^e-\frac{e\mathbf{E}}{m_e}\cdot\nabla_{\mathbf{v}}f^e=C_{ei}(f^e)+C_{ee}(f^e), \tag{2.1}$$

where $\mathbf{E}$ is the electric field, C_{ei} and C_{ee} are electron-ion ($e-i$) and electron-electron ($e-e$) collision terms, respectively. About $\mathbf{E}$ in Eq. (2.1), it can be either a DC electric field, a linearly polarized laser electric field, or a self-generated electrostatic field due to the temperature gradient along the axis z. So we can choose a spherical coordinate system (v,θ,ϕ) in the velocity space and assume that the externally applied or the self-generated electric field is along the z direction as shown in Fig. 1. In this coordinate system all variables are independent of ϕ, therefore, we simplify the velocity space into a two-dimension system (v,θ). For simplification, we also assume the plasma is uniform in x and y direction of configuration space. Finally, the 6-dimensional Eq. (2.1) is simplified into a one-spatial and two-velocity (1D2V) dimensional equation.

Because the mass of ion m_i is much larger than that of electron m_e and usually the thermal velocity of ion v_i is much smaller than that of electron v_e, we can simplify the $e-i$ collision term as [6]

$$C_{ei}=-\nabla_{\mathbf{v}}\cdot\left(-D_{\theta\theta}^{e|i}\mathbf{e}_\theta\mathbf{e}_\theta\cdot\nabla_{\mathbf{v}}f^e\right)=-\nabla_{\mathbf{v}}\cdot\left(-\frac{\Gamma^{e|e}Z_{eff}}{2v}\mathbf{e}_\theta\mathbf{e}_\theta\cdot\nabla_{\mathbf{v}}f^e\right), \tag{2.2}$$

where $D_{\theta\theta}^{e|i}=\Gamma^{e|e}Z_{eff}/2v$ is the diffusion coefficient of $e-i$ collisions in $\mathbf{e}_\theta\mathbf{e}_\theta$ direction with $\Gamma^{e|e}=n_e e^4\ln\Lambda^{e|e}/4\pi\epsilon_0^2 m_e^2$, and $Z_{eff}=-q_i\ln\Lambda^{e|i}/q_e\ln\Lambda^{e|e}\approx Z$ where Z is the ionic charge state. All quantities in the Eq. (2.2) and following equations in this paper are in SI units. In order to handle the processes with highly non-Maxwellian EDFs, the $e-e$ collision

term must be taken into account self-consistently. The fully $e-e$ collision term can be written as a divergence of the particle flux [5–7]

$$C_{ee}=-\nabla_{\mathbf{v}}\cdot\left(-\mathbf{D}^{e|e}\cdot\nabla_{\mathbf{v}}f^e+\mathbf{F}^{e|e}f^e\right)=-\nabla_{\mathbf{v}}\cdot\left(-\frac{\Gamma^{e|e}}{n_e}\nabla_{\mathbf{v}}\nabla_{\mathbf{v}}G^e\cdot\nabla_{\mathbf{v}}f^e+\frac{\Gamma^{e|e}}{n_e}\nabla_{\mathbf{v}}H^ef^e\right), \quad (2.3)$$

where the Rosenbluth potentials are defined by

$$G^e(\mathbf{v})=\frac{1}{2}\int f^e(\mathbf{v}')|\mathbf{v}-\mathbf{v}'|d\mathbf{v}', \quad H^e(\mathbf{v})=\int f^e(\mathbf{v}')|\mathbf{v}-\mathbf{v}'|^{-1}d\mathbf{v}'. \quad (2.4)$$

Decomposing the EDF and the Rosenbluth potentials into the Legendre polynomials as follows [5, 6]

$$f^e(\mathbf{v})=\sum_{l=0}^{\infty}f_l^e(v)P_l(\cos\theta), \quad G^e(\mathbf{v})=\sum_{l=0}^{\infty}G_l^e(v)P_l(\cos\theta), \quad H^e(\mathbf{v})=\sum_{l=0}^{\infty}H_l^e(v)P_l(\cos\theta), \quad (2.5)$$

where the Legendre coefficient of a given EDF can be calculated as

$$f_l^e(v)=\frac{2l+1}{2}\int_0^{\pi}f^e(v,\theta)P_l(\cos\theta)\sin\theta d\theta. \quad (2.6)$$

Given $f_l^e(v)$, we have [5]

$$G_l^e(v)=-\frac{2\pi}{4l^2-1}\left[\int_0^v\frac{(v')^{l+2}}{v^{l-1}}(1-\frac{2l-1}{2l+3}\frac{(v')^2}{v^2})f_l^e(v')dv' + \int_v^{\infty}\frac{v^l}{(v')^{l-3}}(1-\frac{2l-1}{2l+3}\frac{v^2}{(v')^2})f_l^e(v')dv'\right], \quad (2.7)$$

$$H_l^e(v)=\frac{4\pi}{2l+1}\left[\int_0^v\frac{(v')^{l+2}}{v^{l+1}}f_l^e(v')dv'+\int_v^{\infty}\frac{v^l}{(v')^{l-1}}f_l^e(v')dv'\right]. \quad (2.8)$$

Therefore, $\mathbf{D}^{e|e}=D_{vv}^{e|e}\mathbf{e}_v\mathbf{e}_v+D_{v\theta}^{e|e}\mathbf{e}_v\mathbf{e}_\theta+D_{\theta v}^{e|e}\mathbf{e}_\theta\mathbf{e}_v+D_{\theta\theta}^{e|e}\mathbf{e}_\theta\mathbf{e}_\theta$ and $\mathbf{F}^{e|e}=F_v^{e|e}\mathbf{e}_v+F_\theta^{e|e}\mathbf{e}_\theta$ can be calculated efficiently by

$$D_{vv}^{e|e}=\frac{\Gamma^{e|e}}{n_e}\sum_{l=0}^{\infty}\frac{\partial^2G_l^e(v)}{\partial v^2}P_l(\cos\theta), \quad (2.9)$$

$$D_{v\theta}^{e|e}=D_{\theta v}^{e|e}=\frac{\Gamma^{e|e}}{n_e}\sum_{l=0}^{\infty}\left[\frac{1}{v}\frac{\partial G_l^e(v)}{\partial v}-\frac{1}{v^2}G_l^e(v)\right]\frac{\partial P_l(\cos\theta)}{\partial\theta}, \quad (2.10)$$

$$D_{\theta\theta}^{e|e}=\frac{\Gamma^{e|e}}{n_e}\sum_{l=0}^{\infty}\left[\frac{1}{v}\frac{\partial G_l^e(v)}{\partial v}P_l(\cos\theta)+\frac{1}{v^2}G_l^e(v)\frac{\partial^2P_l(\cos\theta)}{\partial\theta^2}\right], \quad (2.11)$$

$$F_v^{e|e}=\frac{\Gamma^{e|e}}{n_e}\sum_{l=0}^{\infty}\frac{\partial H_l^e(v)}{\partial v}P_l(\cos\theta), \quad (2.12)$$

$$F_\theta^{e|e}=\frac{\Gamma^{e|e}}{n_e}\sum_{l=0}^{\infty}\frac{H_l^e(v)}{v}\frac{\partial P_l(\cos\theta)}{\partial\theta}. \quad (2.13)$$

In order to numerically solve Eq. (2.1), at first we take the computational domain as

$$0\le z\le z_{\max},\quad 0\le v\le v_{\max},\quad 0\le\theta\le\pi,$$

then divide z, v and θ into I, M and N equal pieces, respectively. Thus we get the mesh $z_{i-1/2}=i\Delta z$, $(i=0,1,\cdots,I)$; $v_m=m\Delta v$, $(m=0,1,\cdots,M)$; $\theta_n=n\Delta\theta$, $(n=0,1,\cdots,N)$; with step sizes $\Delta z=z_{\max}/I$, $\Delta v=v_{\max}/M$, $\Delta\theta=\pi/N$. This grid system defines a system of cells

$$V_{i,m+1/2,n+1/2}:\ z_{i-1/2}\le z<z_{i+1/2},\ v_m\le v<v_{m+1},\ \theta_n\le\theta<\theta_{n+1},$$

and the EDF is defined at the center of these cells $f_{i,m+1/2,n+1/2}=f(z_i,v_{m+1/2},\theta_{n+1/2})$, where $z_i=(z_{i-1/2}+z_{i+1/2})/2$, $v_{m+1/2}=(v_m+v_{m+1})/2$, $\theta_{n+1/2}=(\theta_n+\theta_{n+1})/2$.

Following the idea of time splitting method, we rewrite the Eq. (2.1) into

$$\frac{\partial f^e}{\partial t}=L_{\mathbf{x}}f^e+L_{\mathbf{v}}f^e, \tag{2.14}$$

$$L_{\mathbf{x}}f^e=-\mathbf{v}\cdot\nabla f^e=-v\cos\theta\frac{\partial f^e}{\partial z}, \tag{2.15}$$

$$L_{\mathbf{v}}f^e=\frac{e\mathbf{E}}{m_e}\cdot\nabla_{\mathbf{v}}f^e+C_{ei}(f^e)+C_{ee}(f^e), \tag{2.16}$$

where $L_{\mathbf{x}}$ and $L_{\mathbf{v}}$ are the differential operators in the configuration and velocity space, respectively. Then the EDF in Eq. (2.14) can be updated with time accuracy $\mathcal{O}(\Delta t^2)$ by the leap-frog time splitting scheme:

(a) update $\partial f^e/\partial t=L_{\mathbf{x}}f^e$ by a half time step $\Delta t/2$;

(b) update $\partial f^e/\partial t=L_{\mathbf{v}}f^e$ by a time step Δt;

(c) update $\partial f^e/\partial t=L_{\mathbf{x}}f^e$ by a half time step $\Delta t/2$ again.

By steps (a)-(c), Eq. (2.14) has been updated by a whole time step, and for the next step $\partial f^e/\partial t=L_{\mathbf{x}}f^e$ and $\partial f^e/\partial t=L_{\mathbf{v}}f^e$ are updated by a reverse order.

2.2 Positive and flux conservative method for the Vlasov equation

In order to strictly preserve the conservation of mass, the positive and flux conservative (PFC) method [3, 4] is applied to update the Vlasov equation part $\partial f^e/\partial t=L_{\mathbf{x}}f^e$ in the configuration space as follows

$$f^e(z_i,v,\theta,t^{k+1})=f^e(z_i,v,\theta,t^k)+\Phi_{i-1/2}(t^k)-\Phi_{i+1/2}(t^k), \tag{2.17}$$

where $\Phi_{i-1/2}$ ($\Phi_{i+1/2}$) is the particle flux through the left (right) boundary of the cell $(z_{i-1/2},z_{i+1/2})$ between $t^k\to t^{k+1}$. With the slope corrector ξ_i to keep the positivity of EDF, we use the second-order approximation to form the EDF in cells as

$$f^e(z)=f_i^e+\xi_i(z-z_i)\frac{f_{i+1}^e-f_i^e}{\Delta z},\quad\forall z\in[z_{i-1/2},z_{i+1/2}], \tag{2.18}$$

Introducing $X=z_{i+1/2}-v\cos\theta\Delta t$ and the integer j that satisfies $z_{j-1/2}<X\leq z_{j+1/2}$, we get the particle flux $\Phi_{i+1/2}$ for the positive propagating velocity $v\cos\theta\geq 0$ as

$$\Phi_{i+1/2}(t^k)=\eta_j\left[f_j+\frac{\xi_j}{2}\left(1-\frac{\eta_j}{\Delta z}\right)(f_{j+1}-f_j)\right]+\Delta z\sum_{k=j+1}^{i}f_k, \tag{2.19}$$

where $\eta_j=z_{j+1/2}-X$, and the slope corrector

$$\xi_j=\begin{cases}\min(1;\,2f_j/(f_{j+1}-f_j)), & \text{if } f_{j+1}>f_j,\\ \min(1;\,-2(f_\infty-f_j)/(f_{j+1}-f_j)), & \text{otherwise,}\end{cases} \tag{2.20}$$

with $f_\infty=\max_{j=0,\cdots,I}f_j$. Similarly, for the negative propagating velocity $v\cos\theta<0$ we have

$$\Phi_{i+1/2}(t^k)=\eta_j\left[f_j-\frac{\xi_j}{2}\left(1+\frac{\eta_j}{\Delta z}\right)(f_j-f_{j-1})\right]+\Delta z\sum_{k=i+1}^{j}f_k, \tag{2.21}$$

where $\eta_j=z_{j-1/2}-X$, and the slope corrector

$$\xi_j=\begin{cases}\min(1;\,2(f_\infty-f_j)/(f_j-f_{j-1})), & \text{if } f_j>f_{j-1},\\ \min(1;\,-2f_j/(f_j-f_{j-1})), & \text{otherwise.}\end{cases} \tag{2.22}$$

2.3 Finite volume method for the Fokker-Planck equation

About the velocity part of VFP, we substitute Eqs. (2.2) and (2.3) into $\partial f^e/\partial t=L_{\mathbf{v}}f^e$, then $L_{\mathbf{v}}f^e$ can be rewritten into a divergence of the particle flux as

$$\frac{\partial f^e}{\partial t}=L_{\mathbf{v}}f^e=-\nabla_{\mathbf{v}}\cdot(J_v\mathbf{e}_v+J_\theta\mathbf{e}_\theta), \tag{2.23}$$

with

$$J_v=-D_{vv}^{e|e}\frac{\partial f^e}{\partial v}-\frac{D_{v\theta}^{e|e}}{v}\frac{\partial f^e}{\partial\theta}+\left(F_v^{e|e}-\frac{eE}{m_e}\cos\theta\right)f^e, \tag{2.24}$$

$$J_\theta=-D_{\theta v}^{e|e}\frac{\partial f^e}{\partial v}-\left(D_{\theta\theta}^{e|e}+\frac{Z_{eff}}{2v}\right)\frac{1}{v}\frac{\partial f^e}{\partial\theta}+\left(F_\theta^{e|e}+\frac{eE}{m_e}\sin\theta\right)f^e. \tag{2.25}$$

Then the finite volume method [5], which is similar to the finite difference method [6], is applied to update Eq. (2.23). Because in the finite volume method the integral form is used instead to discretize the equation, the finite volume method can self-consistently avoid the singularity at internal boundaries $v=0$, $\theta=0$, and $\theta=\pi$ in comparison with the finite difference method [8]. The finite volume method also preserves the particle

number conservation strictly. Integrating Eq. (2.23) upon the cells $V_{m+1/2,n+1/2}$ in the velocity space, we get

$$V_{m+1/2,n+1/2}\frac{\partial f^e_{m+1/2,n+1/2}}{\partial t}=-[S_{m+1,n+1/2}J_{v,m+1,n+1/2}-S_{m,n+1/2}J_{v,m,n+1/2} +S_{m+1/2,n+1}J_{\theta,m+1/2,n+1}-S_{m+1/2,n}J_{\theta,m+1/2,n}], \quad (2.26)$$

where $V_{m+1/2,n+1/2}=2\pi(v^3_{m+1}-v^3_m)(\cos\theta_n-\cos\theta_{n+1})/3$ is the volume of cell, $S_{m,n+1/2}=2\pi(\cos\theta_n-\cos\theta_{n+1})v^2_m$ and $S_{m+1/2,n}=\pi(v^2_{m+1}-v^2_m)\sin\theta_n$ are the surfaces of cell perpendicular and parallel to the v axis, respectively. It is convenient to divide the Eq. (2.26) into three pieces

$$\frac{\partial f^e_{m+1/2,n+1/2}}{\partial t}+(A_v+A_\theta+A_\times)f^e_{m+1/2,n+1/2}=0, \quad (2.27)$$

where the derivative along v direction A_v, the derivative along θ direction A_θ, and the cross derivative $A_\times$ are given by

$$(A_vf)_{m+1/2,n+1/2}=a_vf^e_{m-1/2,n+1/2}+b_vf^e_{m+1/2,n+1/2}+c_vf^e_{m+3/2,n+1/2}, \quad (2.28)$$

$$(A_\theta f)_{m+1/2,n+1/2}=a_\theta f^e_{m+1/2,n-1/2}+b_\theta f^e_{m+1/2,n+1/2}+c_\theta f^e_{m+1/2,n+3/2}, \quad (2.29)$$

$$\begin{aligned}(A_\times f)_{m+1/2,n+1/2}=&a_\times f^e_{m-1/2,n-1/2}+b_\times f^e_{m-1/2,n+1/2}+c_\times f^e_{m-1/2,n+3/2}\\&+d_\times f^e_{m+1/2,n-1/2}+e_\times f^e_{m+1/2,n+3/2}\\&+f_\times f^e_{m+3/2,n-1/2}+g_\times f^e_{m+3/2,n+1/2}+h_\times f^e_{m+3/2,n+3/2},\end{aligned} \quad (2.30)$$

with

$$a_v=B_{v,m}\Big[-\frac{D^{e|e}_{vv}}{\Delta v}-(F^{e|e}_v-\frac{eE\cos\theta}{m_e})\delta\Big]_{m,n+1/2}, \quad (2.31)$$

$$\begin{aligned}b_v=&B_{v,m}\Big[\frac{D^{e|e}_{vv}}{\Delta v}-(F^{e|e}_v-\frac{eE\cos\theta}{m_e})\epsilon\Big]_{m,n+1/2}\\&+B_{v,m+1}\Big[\frac{D^{e|e}_{vv}}{\Delta v}+(F^{e|e}_v-\frac{eE\cos\theta}{m_e})\delta\Big]_{m+1,n+1/2},\end{aligned} \quad (2.32)$$

$$c_v=B_{v,m+1}\Big[-\frac{D^{e|e}_{vv}}{\Delta v}+(F^{e|e}_v-\frac{eE\cos\theta}{m_e})\epsilon\Big]_{m+1,n+1/2}, \quad (2.33)$$

$$a_\theta=B_{\theta,n}\Big[-\frac{2vD^{e|e}_{\theta\theta}+Z}{2v^2\Delta\theta}-(F^{e|e}_\theta+\frac{eE\sin\theta}{m_e})\delta\Big]_{m+1/2,n}, \quad (2.34)$$

$$\begin{aligned}b_\theta=&B_{\theta,n}\Big[\frac{2vD^{e|e}_{\theta\theta}+Z}{2v^2\Delta\theta}-(F^{e|e}_\theta+\frac{eE\sin\theta}{m_e})\epsilon\Big]_{m+1/2,n}\\&+B_{\theta,n+1}\Big[\frac{2vD^{e|e}_{\theta\theta}+Z}{2v^2\Delta\theta}+(F^{e|e}_\theta+\frac{eE\sin\theta}{m_e})\delta\Big]_{m+1/2,n+1},\end{aligned} \quad (2.35)$$

$$c_\theta = B_{\theta,n+1}\Big[-\frac{2vD^{e|e}_{\theta\theta}+Z}{2v^2\Delta\theta}+(F^{e|e}_\theta+\frac{eE\sin\theta}{m_e})\epsilon\Big]_{m+1/2,n+1}, \tag{2.36}$$

$$a_\times = -B_{v,m}\frac{\delta D^{e|e}_{v\theta}}{2v\Delta\theta}\bigg|_{m,n-1/2} - B_{\theta,n}\frac{\delta D^{e|e}_{\theta v}}{2\Delta v}\bigg|_{m-1/2,n}, \tag{2.37}$$

$$b_\times = B_{\theta,n} - \frac{\epsilon D^{e|e}_{\theta v}}{2\Delta v}\bigg|_{m-1/2,n} + B_{\theta,n+1}\frac{\delta D^{e|e}_{\theta v}}{2\Delta v}\bigg|_{m-1/2,n+1}, \tag{2.38}$$

$$c_\times = B_{v,m}\frac{\delta D^{e|e}_{v\theta}}{2v\Delta\theta}\bigg|_{m,n+3/2} + B_{\theta,n+1}\frac{\epsilon D^{e|e}_{\theta v}}{2\Delta v}\bigg|_{m-1/2,n+1}, \tag{2.39}$$

$$d_\times = -B_{v,m}\frac{\epsilon D^{e|e}_{v\theta}}{2v\Delta\theta}\bigg|_{m,n-1/2} + B_{v,m+1}\frac{\delta\Delta D^{e|e}_{v\theta}}{2v\theta}\bigg|_{m+1,n-1/2}, \tag{2.40}$$

$$e_\times = B_{v,m}\frac{\epsilon D^{e|e}_{v\theta}}{2v\Delta\theta}\bigg|_{m,n+3/2} - B_{v,m+1}\frac{\delta D^{e|e}_{v\theta}}{2v\Delta\theta}\bigg|_{m+1,n+3/2}, \tag{2.41}$$

$$f_\times = B_{v,m+1}\frac{\epsilon D^{e|e}_{v\theta}}{2v\Delta\theta}\bigg|_{m+1,n-1/2} + B_{\theta,n}\frac{\delta D^{e|e}_{\theta v}}{2\Delta v}\bigg|_{m+3/2,n}, \tag{2.42}$$

$$g_\times = B_{\theta,n}\frac{\epsilon D^{e|e}_{\theta v}}{2\Delta v}\bigg|_{m+3/2,n} - B_{\theta,n+1}\frac{\delta D^{e|e}_{\theta v}}{2\Delta v}\bigg|_{m+3/2,n+1}, \tag{2.43}$$

$$h_\times = -B_{v,m+1}\frac{\epsilon D^{e|e}_{v\theta}}{2v\Delta\theta}\bigg|_{m+1,n+3/2} - B_{\theta,n+1}\frac{\epsilon D^{e|e}_{\theta v}}{2\Delta v}\bigg|_{m+3/2,n+1}, \tag{2.44}$$

where $B_{v,m}=S_{m,n+1/2}/V_{m+1/2,n+1/2}$, $B_{\theta,n}=S_{m+1/2,n}/V_{m+1/2,n+1/2}$, and $\epsilon=1-\delta$. The factors δ are introduced to evaluate f^e at the cell edges [9], and they can be calculated as

$$\delta_{m,n+1/2} = g(-\Delta v F^{e|e}_{v,m,n+1/2}/D^{e|e}_{vv,m,n+1/2}), \tag{2.45}$$

$$\delta_{m+1/2,n} = g(-\Delta\theta F^{e|e}_{\theta,m+1/2,n}/D^{e|e}_{\theta\theta,m+1/2,n}), \tag{2.46}$$

with $g(x)=1/x-1/[\exp(x)-1]$. Finally, we use the alternating-direction-implicit method [10] to advance Eq. (2.27) in time by the following steps:

(a) calculate ς^k as $\varsigma^k=-(A_v+A_\theta+A_\times)f^e(t^k)$;

(b) solve $\varsigma^{k+1/2}$ from $(I+A_v\Delta t/2)\varsigma^{k+1/2}=\varsigma^k$;

(c) solve ς^{k+1} from $(I+A_\theta\Delta t/2)\varsigma^{k+1}=\varsigma^{k+1/2}$;

(d) finally get $f^e(t^{k+1})=f^e(t^k)+\Delta t\varsigma^{k+1}$.

3 Vlasov-Fokker-Planck simulations for selected problems in high-power laser plasmas

3.1 The generation of plasma current in a strong DC electric field

It is well known that a DC electric field will produce a current in a plasma. If the field is weak enough, the produced current can be calculated by Spitzer-Härm's theory [1]

$$\mathbf{J}=\sigma\mathbf{E}, \tag{3.1}$$

with the plasma electric conductivity $\sigma\propto T_e^{3/2}$. However, Spitzer-Härm's theory is based on the perturbation theory and assumes the existence of an approximation to a Maxwellian EDF. Therefore, it is valid only for $E\ll E_c=m_{e0}v_e\nu_{ei}/e$, where E_c is the so-called runaway field, $\nu_{ei}=Z\Gamma^{e|e}/v_{e0}^3$ is the $e-i$ collision frequency with the initial thermal velocity v_{e0}, and $\tau_{ei}=1/\nu_{ei}$ is the mean $e-i$ collision time. However, the electron kinetics are very complex and the observed electric conductivities are usually much lower than that predicted by Spitzer-Härm in the non-weak fields [11]. In this subsection, plasma kinetics in a DC electric field is studied with a wide range of field strength. After that a set of hydrodynamic-like equations are introduced for calculating the generated plasma current as well as parallel and perpendicular temperatures in a strong DC electric field.

The VFP equation (2.1) of a homogeneous plasma in a DC electric field can be simplified into the so-called Fokker-Planck (FP) equation [5,6,12,13]

$$\frac{\partial f^e}{\partial t}=\frac{e\mathbf{E}}{m_e}\cdot\nabla_{\mathbf{v}}f^e+C_{ei}(f^e)+C_{ee}(f^e). \tag{3.2}$$

Compared with the VFP equation, the FP equation only contains L_v in the velocity space, so it can be numerically solved by the finite volume method.

As shown in Fig. 2 obtained by numerical solution of Eq. (3.2), the produced plasma current in a very weak field will achieve a steady value after a short response time. If we define the plasma electric conductivity as the ratio of this steady current to the electric field, it is found that the conductivities obtained from our simulations show a good quantitative agreement with the values estimated by Spitzer-Härm's transport theory for different ionic charge states Z in this weak field (Table 1). Defining the response time (the relaxation time) as the time needed to generate (damp) the current as large as $\sigma E(1-1/e)$ (here e is Euler's number), we find that the response time to generate the current in a weak DC electric field is equal to the relaxation time after turning off this field as shown in Table 1. This illustrates that the perturbation of this weak field upon the EDF is small enough for the application of Spitzer-Härm's theory, and the perturbed EDF can return to the equilibrium Maxwellian distribution as quickly as it departs.

In contrast with the EDF approximately satisfying the Maxwellian distribution in a weak DC electric field, it may far depart from the Maxwellian distribution in a strong DC field, which can obviously modify the plasma electric conductivity as well as other

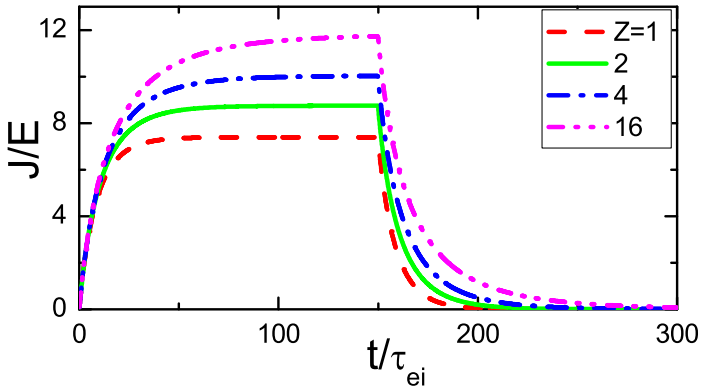

Figure 2: The generations of plasma currents with different ionic charge states Z in a very weak DC electric field $E=1\times10^{-5}E_c$ and the attenuations of these currents after turning off the electric field at $t=150\tau_{ei}$. The initial EDFs satisfy the Maxwellian distribution, J/E is in unit of $n_e e^2\tau_{ei}/m_e$.

Table 1: Electric conductivity obtained from FP simulation σ_{FP} and that given by Spitzer-Härm σ_{SH}; the response time τ_{r1} to generate current and the relaxation time τ_{r2} to damp current. The parameters are as in Fig. 2.

Z	1	2	4	10	16	100
σ_{FP}	7.393	8.747	10.03	11.20	11.73	12.21
σ_{SH}	7.427	8.726	10.02	-	11.78	-
τ_{r1}/τ_{ei}	8.7	10.9	13.3	15.7	17.0	17.9
τ_{r2}/τ_{ei}	8.7	10.9	13.2	15.7	17.0	18.3

properties. For example, the time evolution of the EDF in a non-weak field $E=0.2E_c$ is shown in Fig. 3. It is found that the initial stationary Maxwellian EDF will evolve into a hybrid of one stationary Maxwellian EDF and another drifting Maxwellian EDF in this field. In this process, the proportion of the drifting Maxwellian EDF and the mean drift velocity both increase. The similar process happens in a very strong DC electric field, but the drifting Maxwellian distribution can quickly dominate after a few collision

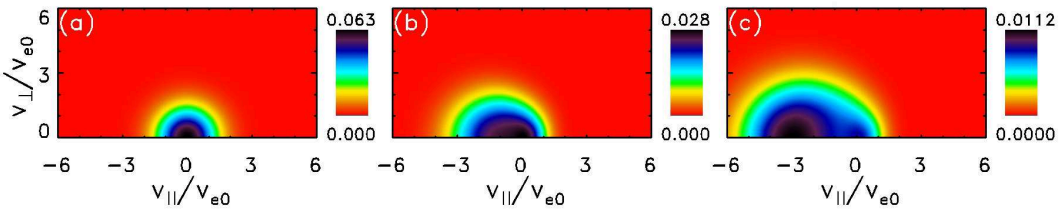

Figure 3: The time evolution of the EDF in a DC electric field $E=0.2E_c$. (a) $t=0$, (b) $t=10\tau_{ei}$, and (c) $t=20\tau_{ei}$. The EDF is in unit of n_e/v_{e0}^3 and ionic charge state $Z=1$. For convenience of visualization, the EDFs are drawn in cylindrical coordinates $(v_{\parallel}=v\cos\theta, v_{\perp}=v\sin\theta)$.

periods [14]. Both the stationary Maxwellian distribution and the drifting Maxwellian distribution can be considered as the special cases of this hybrid distribution, therefore, the general EDF at any time in a DC electric field can be expressed as [14]

$$f(\mathbf{v})=\chi\frac{n_e}{(2\pi v_{te1}^2)^{3/2}}\exp\left(-\frac{v^2}{2v_{te1}^2}\right)+(1-\chi)\frac{n_e}{(2\pi v_{te2}^2)^{3/2}}\exp\left[-\frac{(\mathbf{v}-\mathbf{v_d})^2}{2v_{te2}^2}\right], \tag{3.3}$$

where χ is the proportion of the stationary Maxwellian component, the first and second terms of RHS are the stationary and the drifting Maxwellian components, respectively.

If we define the parallel temperature as $T_\parallel = m_e\int f(\mathbf{v})v_\parallel^2 d\mathbf{v}$ and the perpendicular temperature as $T_\perp = m_e\int f(\mathbf{v})v_\perp^2 d\mathbf{v}/2$, it will be a good approximation to calculate plasma current as [14]

$$\begin{aligned}J=&\sigma_0 E\left[1-\exp\left(-\frac{t}{\tau_{r1}}\right)\right]\exp\left(\frac{T_\perp-T_\parallel}{T_\perp}\right)\left(\frac{T_\perp}{T_0}\right)^{3/2}\\&+n_e e\left[1-\exp\left(\frac{T_\perp-T_\parallel}{T_\perp}\right)\right]\left(\frac{T_\parallel-T_\perp}{m_e}\right)^{1/2},\end{aligned} \tag{3.4}$$

where the first term is attributed to the stationary component, the second term is attributed to the drifting Maxwellian component, τ_{r1} is the response time and σ_0 is Spitzer-Härm's electric conductivity [1] for initial temperature T_0 as listed in Table 1. According to the ohmic heating [15] and the relaxation of the anisotropic temperature [13, 16], the parallel temperature $T_\parallel$ and the perpendicular $T_\perp$ can be approximately updated as

$$\frac{dT_\parallel}{dt}=2JE-2\nu_{ei}(v_{eff})(T_\parallel-T_\perp), \tag{3.5}$$

$$\frac{dT_\perp}{dt}=\nu_{ei}(v_{eff})(T_\parallel-T_\perp), \tag{3.6}$$

with the effective $e-i$ collision frequency $\nu_{ei}(v_{eff})=Z\Gamma^{e|e}/v_{eff}^3$ and the effective electron thermal velocity $v_{eff}=[(T_\parallel^2+2T_\perp^2)/m_e]^{1/2}$.

In the weak field limit, the temperature isotropization is much faster than the ohmic heating as indicated by Eqs. (3.5)-(3.6). In this case $T_\parallel = T_\perp = T$ satisfies well, then Eqs. (3.4)-(3.6) will degenerate to Spitzer-Härm's model

$$J=\sigma_0 E\left[1-\exp(-\frac{t}{\tau_r})\right]\left(\frac{T}{T_0}\right)^{3/2}, \tag{3.7}$$

$$\frac{dT}{dt}=\frac{2}{3}JE. \tag{3.8}$$

From hydrodynamic-like Eqs. (3.4)-(3.6) with the initial plasma parameters, one can follow the time evolution of the generated plasma current as well as the parallel temperature $T_\parallel$ and the perpendicular temperature $T_\perp$ under a DC electric field with different

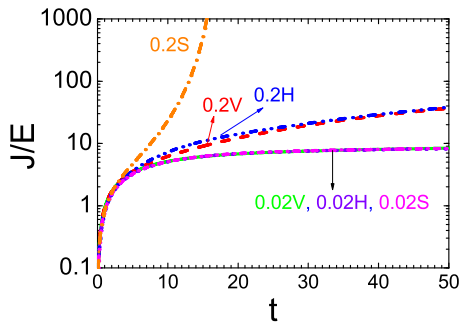

Figure 4: The time evolution of the generated plasma currents in a weak DC electric field $0.02E_c$ and a non-weak DC electric field $0.2E_c$. The currents calculated by our hydrodynamic-like Eqs. (3.4)-(3.6) are marked as 0.02H and 0.2H, the currents by Spitzer-Härm's model are marked as 0.02S and 0.2S, and the currents obtained from the VFP code are marked as 0.02V and 0.2V. J/E is in unit of $n_e e^2 \tau_{ei}/m_e$, t is in unit of τ_{ei}, and $Z=1$.

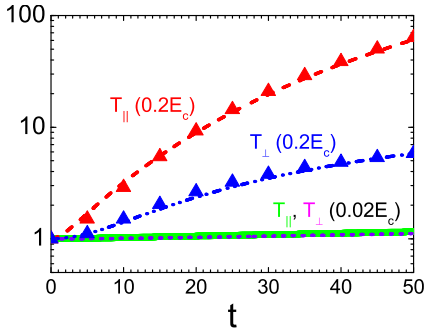

Figure 5: The parallel and the perpendicular temperatures in a weak DC electric field $0.02E_c$ and a non-weak DC electric field $0.2E_c$. The curves are the results from VFP simulations. The results obtained from hydrodynamic-like Eqs. (3.4)-(3.6) are drawn as triangles at $E=0.2E_c$ for comparison. The parallel and perpendicular temperatures are normalized to the initial temperature $T_0 = m_e v_{e0}^2$, and t is in unit of τ_{ei}.

strengths as shown in Fig. 4 and Fig. 5. It is found that the ohmic heating is inefficient in the weak field $0.02E_c$, so $e-i$ collisions can keep the EDF almost isotropic in this case, i.e. $T_\parallel = T_\perp = T$ (see Fig. 5). As a result, the generated plasma current is well described by Spitzer-Härm's model. While in the non-weak field $0.2E_c$ the ohmic heating is so efficient that an obvious divergence between $T_\parallel$ and $T_\perp$ appears (see Fig. 5). Consequently, Spitzer-Härm's model highly overestimates the generated plasma current (see Fig. 4). Since our hydrodynamic-like Eqs. (3.4)-(3.6) can well follow the divergence between $T_\parallel$ and $T_\perp$ (see Fig. 5), they are competent to describe the time evolution of the generated plasma current well in this non-weak field $0.2E_c$ (see Fig. 4). This illustrates the hydrodynamic-like Eqs. (3.4)-(3.6) is free from the weak-field limit and more suitable for application in hybrid-particle-in-cell simulations in the high field regime such as in the fast ignition scheme of the inertial confinement fusion (ICF) [17, 18]. As discussed in [14], the hydrodynamic-like Eqs. (3.4)-(3.6) is competent to handle the return current generation and the relevant ohmic heating during a big current of fast electron beam transporting in the fast ignition targets.

Furthermore, we compare the generations of plasma currents in DC electric fields with different strengths and the attenuations of currents after turning off these electric fields in Fig. 6. It is found that there is a clear response process for generating the current in the weak DC electric field $E=0.02E_c$, and the relaxation time for attenuating the current after turning off the filed is almost equal to the response time. While in the non-weak field $0.2E_c$ the generated current grows faster and faster due to the efficient ohmic heating. Meanwhile, the effective $e-i$ collision frequency $\nu_{ei}(v_{eff})$ decreases greatly with the quickly increasing $T_\parallel$ in the strong field. Therefore, after switching off the strong electric field the relaxation of the anisotropy such as the damping of current is much slower than the generation process.

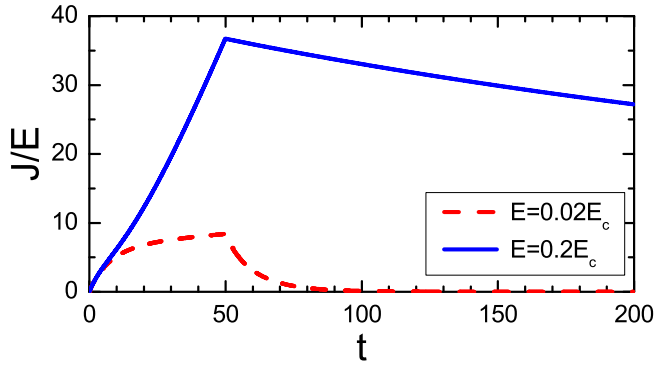

Figure 6: The generation of plasma currents in DC electric fields with different strengths and the attenuation of currents after turning off these electric fields at $t=50\tau_{ei}$. The initial EDFs satisfy the Maxwellian distribution, J/E is in unit of $n_e e^2\tau_{ei}/m_e$, and t is in unit of τ_{ei}.

3.2 IB absorption at high laser intensity

In contrast to the plasma current that induced by a DC electric field, the IB absorption occurs in the alternating current (AC) electric field of laser pulse. Except that the DC electric field is replaced by the laser electric field **E**, the evolution of the EDF in a homogeneous plasma and the IB absorption can be described by the Fokker-Planck equation in the same form as Eq. (3.2). By solving this equation numerically, we have investigated the IB absorption with self-consistent $e-e$ and $e-i$ collision operators in earlier studies [5].

In large scale simulations for the ICF research, it often requires to have the laser absorption and the electron heat transport obtained from the VFP simulation coupled to hydrodynamic codes. It is thus desirable to have a simplified model to calculate the IB absorption. For this purpose, the well-known Langdon IB operator was designed [2], which can treat the IB absorption consistently with the evolution of the EDF. But Langdon's IB operator is based on the perturbation theory and assumes the weak anisotropy of the EDF as Spitzer-Härm's theory. Therefore, it is only valid for $E_L \ll m_e v_e \omega/e$ i.e. $u_0 \ll v_e$ ($u_0 = eE_L/m_e\omega$ is the quiver velocity of electrons in the laser field E_L, v_e is the electron thermal velocity, and ω is the laser frequency). Consequently, it is expected that Langdon's IB operator is valid only for a high enough plasma temperature and a low enough laser intensity. It may overestimate the absorption rate at a low plasma temperature or at a moderate or high intensity [19], which may relate to the ICF schemes. Particularly for shock ignition [20] and impact ignition ICF [21] the applied laser intensity can be as high as 10^{16} W/cm^2, and the IB absorption may still be one of the most important laser energy deposition mechanisms at this intensity since $\lambda^2 I < 10^{17}$ μm^{2}W/cm^2 [22–25]. However, Langdon's IB operator sometimes is still used to treat IB absorption at this moderate laser intensity regardless of the ratio u_0/v_e [26]. In this subsection, based upon our VFP simulation [5], a modified IB operator will be introduced for dealing with the nonlinear IB absorption consistently with the evolution of the EDF at low plasma temperature and the high laser intensity.

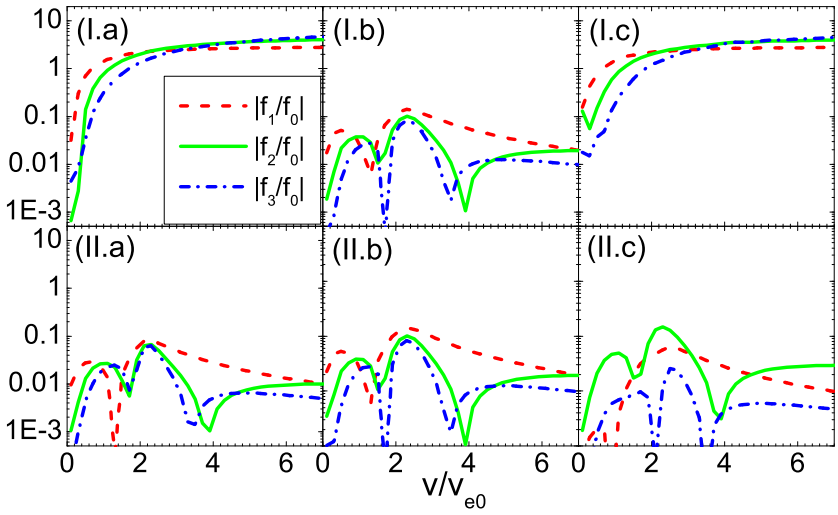

Figure 7: Legendre expansion coefficients of the EDF obtained from the VFP simulations in an intense laser field at three representative times: (a) 1/4 laser cycle, (b) 1/2 laser cycle, (c) 3/4 laser cycle. The first row is obtained from the rest laboratory frame, while the second row is the results in the oscillating comoving frame. f_l is the l-order Legendre expansion coefficient of EDF, Legendre coefficients are normalized to the isotropic part of the EDF f_0, and v_{e0} is the initial thermal velocity. The plasmas and laser parameters are: electron density $n_e=10^{20}$ cm^{-3}, initial temperature $T_e=1$ keV, ionization state $Z=1$, laser wavelength $\lambda=1.06$ μm, and intensity $I=10^{16}$ W/cm^2 with $u_0\simeq 2.0v_{e0}$.

Since the EDF oscillates with the amplitude u_0 in an intense laser, it is obvious that the assumption of weak anisotropy, i.e. $|f_2|\ll|f_1|\ll|f_0|$, can not be always satisfied in the rest laboratory frame if $u_0>v_e$ as shown in Figs. 7(Ia)-(Ic). Fortunately, this assumption can be always well satisfied in the comoving frame with oscillating velocity $\mathbf{u}=-u_0\sin(\omega t)\mathbf{e}_z$ as shown in Figs. 7(IIa)-(IIc). So we can use the transformation $\mathbf{v}'=\mathbf{v}-\mathbf{u}$ and rewrite Eq. (3.2) in the oscillating comoving coordinate system (v',θ') as [27]

$$\frac{\partial f'}{\partial t}=C'_{ei}(f')+C'_{ee}(f'), \tag{3.9}$$

where $C'_{ee}(f')$ is identical to $C_{ee}(f^e)$ due to the invariance of the self-collision term under coordinate transformation; while the $e-i$ collision operator in the comoving coordinate system should be modified as

$$C'_{ei}(f')=\frac{\nu_{ei}(u,v',\theta')}{2}\left[\frac{u^2+2uv'\cos\theta'+u^2\cos^2\theta'}{v'}\frac{\partial f'}{\partial v'}+\frac{v'^2+2uv'\cos\theta'+u^2\cos 2\theta'}{v'^2\tan\theta'}\frac{\partial f'}{\partial\theta'}\right.$$
$$\left.+(u\sin\theta')^2\frac{\partial^2 f'}{\partial v'^2}+\left(\frac{v'+u\cos\theta'}{v'}\right)^2\frac{\partial^2 f'}{\partial\theta'^2}+\frac{2u\sin\theta'(v'+u\cos\theta')}{v'}\frac{\partial^2 f'}{\partial v'\partial\theta'}\right], \tag{3.10}$$

where the temporary effective $e-i$ collision frequency is given by

$$\nu_{ei}(u,v',\theta')=\frac{Z\Gamma^{e|e}}{(u^2+2uv'\cos\theta'+v'^2)^{3/2}}. \tag{3.11}$$

Meanwhile it is more suitable to calculate the Coulomb logarithm $\ln\Lambda$ by $(v_e^2+u_0^2/4)^{1/2}$ instead of v_e at high laser intensity [28,29].

Since the fast oscillation has been transformed into the comoving coordinate system, the EDF appears to be nearly isotropic in the comoving coordinate frame regardless of the laser intensity as shown in Fig. 7(IIa)-(IIc). So it is a good approximation to decompose the EDF into Legendre polynomials $P_l(\cos\theta')$ and retain only the first two terms as

$$f'(v',\theta') \simeq f_0'(v') + f_1'(v')\cos\theta'. \tag{3.12}$$

If $\omega \gg \nu_{ei}$ (which is usually fulfilled in laser-plasma interactions), we can assume $\partial f_1'/\partial t \simeq -i\omega f_1'$ and follow the process of deducing Langdon's operator, and then get

$$\frac{\partial f_0'}{\partial t} \simeq \frac{u^2}{3v'^2}\frac{\partial}{\partial v'}\left[v'^2\nu_{ei}' g(\nu_{ei}')\frac{\partial f_0}{\partial v'}\right] + C_0', \tag{3.13}$$

where $g(\nu_{ei}') = 1 - b(\nu_{ei}'/\omega)^2/[1+b^2(\nu_{ei}'/\omega)^2]$ with $\nu_{ei}' = Z\Gamma^{e|e}/(u^2+v'^2)^{3/2}$ and $b = (2u^2+5v'^2)/5v'^2$; while C_0' is the $e-e$ collision term only relevant to f_0' that can be calculated by Eqs. (26)-(27) in the [6].

However, it is still difficult to analytically average the Eq. (3.13) over one laser cycle for arbitrary ratios u_0/v_e. With the help of numerical simulations, fortunately, we find the following equation [27]

$$\frac{\partial f_0'}{\partial t} \simeq \frac{u_0^2}{6v'^2}\frac{\partial}{\partial v'}\left[v'^2\nu_{eff}' g(\nu_{eff}')\frac{\partial f_0}{\partial v'}\right] + C_0', \tag{3.14}$$

can generate the absorption rate in good quantitative agreement with that obtained from our FP code for a wide range of laser intensity and plasma temperature, where

$$g_0(\nu_{eff}') = 1 - b_0(\nu_{eff}'/\omega)^2/[1+b_0^2(\nu_{eff}'/\omega)^2], \tag{3.15}$$

with $b_0 = (u_0^2+5v'^2)/5v'^2$ and $\nu_{eff}' = Z\Gamma^{e|e}/(v'^2+u_0^2/\zeta)^{3/2}$, the coefficient ζ is numerically fitted as

$$\zeta = 3.84 + \frac{142.59 - 65.48u_0/v_e}{27.3u_0/v_e + (u_0/v_e)^2}. \tag{3.16}$$

In [27], we have discussed the IB absorption and the validity of Langdon's and our IB operators in different laser intensity regimes. In this paper, we continue to compare the absorption rates obtained from different methods as functions of the plasma temperature as shown in Fig. 8. The result from the molecular dynamic simulation [30] is drawn again for comparison because it avoids most of the assumptions used in other methods and thus provides reliable tests. Here we use the fixed laser intensity $I = 2\times10^{15}$. For this laser intensity, $u_0 \ll v_e$ only holds for a high plasma temperature $T_e \gg 840$ eV. As a result, the absorption rate obtained from Langdon's IB operator is an order of magnitude larger than those obtained from other methods for a relative cold plasma temperature $T_e < 100$

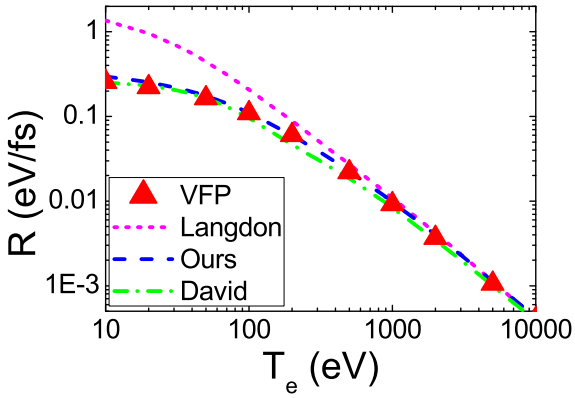

Figure 8: The absorption rates R as functions of the plasma temperature obtained from VFP code (triangle), Langdon's IB operator (short dashed line), our IB operator (dashed line), and David's fitted formula (6) in [30] from molecular dynamic method (dash-dotted line). The absorption rate is defined as the increase rate of electron temperature averaged over the first four laser cycles. The simulation parameters are: plasma density $n_e=10^{20}$ cm^{-3}, $Z=1$, laser intensity $I=2\times10^{15}$ W/cm^2, and laser wavelength $\lambda=1.06\mu$m.

eV. Even at a quite high temperature $T_e=1000$ eV, Langdon's IB operator still results in a relative error as large as 28.3%. While our IB operator results in a rational absorption rate at the whole plasma temperature range, which has a very good quantitative agreement (relative error always $<14.0\%$) with VFP simulation and the molecular dynamic simulation [30]. It illuminates that instead of Langdon's operator our IB operator can be used to handle the IB absorption in a not-so-hot plasma in the early and middle stage of the heating in the ICF schemes. Therefore, our IB operator can be considered as the generalized version of Langdon's IB operator to be conveniently integrated into multi-spatial dimensional Fokker-Planck codes for a variety of practical applications [31].

3.3 Nonlocal heat transport in laser-produced plasmas

As the produced plasma current in a low DC electric field satisfies Spitzer-Härm electric transport theory, the heat flux q under a small temperature gradient ∇T can also be described by Spitzer-Härm heat transport theory as

$$q_{\rm SH}=-\kappa\nabla T_e=-\gamma_Z\kappa_L\nabla T_e, \tag{3.17}$$

where κ is the heat conductivity [1] and the Lorentz heat conductivity κ_L is given by

$$\kappa_L=256\frac{\sqrt{2\pi}\varepsilon_0^2m_e^2}{Ze^4\ln\Lambda}\left(\frac{k_BT_e}{m_e}\right)^{5/2}, \tag{3.18}$$

and $\gamma_Z=\kappa/\kappa_L$ is the normalized heat conductivity for ionic charge state Z. Since Spitzer-Härm theory is a perturbation theory assuming the Maxwellian EDF, it is valid only for a very small temperature gradient $\lambda_e/L\ll2\times10^{-3}$ [32], where $\lambda_{ei}=v_{te}/\nu_{ei}$ is the electron mean free path and $L=T_e/\nabla T_e$ is the scale length of temperature gradient.

However, with the increase of the available laser power, very steep temperature gradients often occur in the laser-produced plasmas, especially near the critical surface [33]. As a result, the experimentally observed heat flux near the critical surface is usually much smaller than that predicted by Spitzer-Härm's theory [33–35]. This phenomenon is called as "flux inhibition". In the early years, a simple flux limiter [36] was introduced into the Spitzer-Härm transport theory to handle this phenomenon. However, this method belongs to the hydrodynamical description and it cannot describe the "preheat" by the hot electrons which stream from the main body of the heat front with a longer electron mean free path [37]. Therefore, many nonlocal thermal transport models with different delocalized convolutions [32,38–41] have been designed to describe the "preheat", which can be conveniently integrated into the hydrodynamic codes and improve their accuracy. However, only a few nonlocal thermal transport models [41] can partially describe the "preheat" quantitatively accurately. Therefore, in order to study the nonlocal heat transport as accurately as possible, we develop an one-spatial-dimensional and two-velocity-dimensional (1D2V) VFP simulation code, which numerically solve the kinetic Eq. (2.1) self-consistently by the scheme described in Section 2.

In the simulations of this subsection, we assume that the plasma temperature is uniform along x and y directions. And if no special explanation is given, we use the uniform density $n_0 = 10^{21}$ cm^{-3}, which is close to the critical density for 1 μm laser wavelength. The temperature profile along z direction is given by

$$T_e(z) = \begin{cases} T_0, & \text{if } z > 2z_{\max}/3, \\ T_0 + 2\Delta T, & \text{if } z < z_{\max}/3, \\ T_0 + \Delta T + \Delta T \cos[(3z/z_{\max} - 1)\pi], & \text{otherwise}, \end{cases} \tag{3.19}$$

as shown in Fig. 9, where we take the reflected boundary condition. The initial simulation conditions with the different temperature gradient can be achieved by varying the parameters T_0, ΔT or $z_{\max}$ in Eq. (3.19). We also assume that the initial EDF at every position satisfies the local Maxwellian distribution.

With $T_0 = 100$ eV, $\Delta T = 10^{-8} T_0$ and $z_{\max} = 300$ μm, we examine the heat transport under a very small temperature gradient. In Fig. 10, we show the time evolution of the heat flux at $z = z_{\max}/2$ for plasmas with different ionic charge state Z. Since we use the initial Maxwellian EDF, the generation of heat flux also needs a response time as well as the generation of plasma current discussed in Section 3.1. Defining the normalized heat conductivity as the ratio of this steady flux to $q_L = -K_L \nabla T_e$ and the response time as the time to generate the heat flux as large as $(1-1/e)$ of the steady value (here e is Euler's number), we show the normalized heat conductivities and the response times for some different ion charge states in Table 2.

For such a small temperature gradient $\lambda_{ei}/L \leq 6 \times 10^{-11} \ll 2 \times 10^{-3}$ holds at the whole computational region, the Spitzer-Härm heat transport theory should be well valid, and the heat flux should be proportional to the temperature gradient. But we have found that although the obtained heat flux is well proportional to the temperature gradient at the whole computational region, there is an obvious divergence between the coefficients

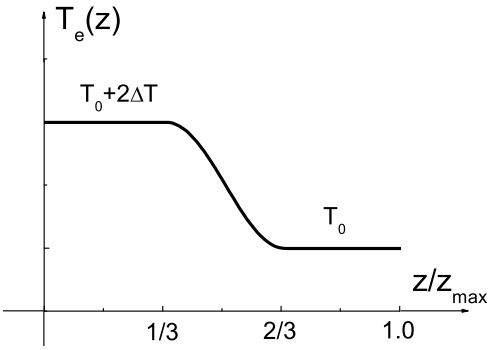

Figure 9: The initial temperature profile used in Figs. 10-16, The initial simulation conditions with the different temperature gradient can be achieved by varying the parameters T_0, ΔT or $z_{\max}$.

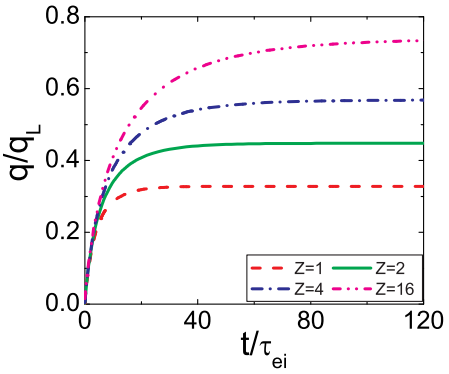

Figure 10: Time evolution of heat flux at $z=z_{\max}/2$ for plasmas with different Z under a very small temperature gradient with T_0=100 eV, $\Delta T=10^{-8}T_0$ and $z_{\max}$=300 μm. Heat flux is in unit of $q_L=-K_L\nabla T_e$.

Table 2: The normalized heat conductivity given by Spitzer-Härm $\gamma_{\rm SH}$ and that obtained from our VFP simulation $\gamma_{\rm VFP}$, and the response time τ_q for different ionic charge states Z.

Z	1	2	4	16
$\gamma_{\rm SH}$	0.2358	0.3652	0.5142	0.7826
$\gamma_{\rm VFP}$	0.3305	0.4506	0.5719	0.7434
τ_q/τ_{ei}	4.2	6.4	9.1	14.2

(heat conductivity) that obtained from Spitzer-Härm's model and the VFP simulation as shown in Fig. 11. The detailed difference between the normalized heat conductivities obtained from VFP simulations $\gamma_{\rm VFP}$ and these estimated by Spitzer-Härm $\gamma_{\rm SH}$ is shown

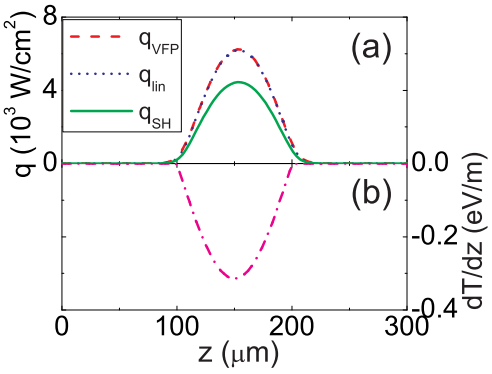

Figure 11: (a) $q_{\rm SH}$ from Spitzer-Härm's model [Eq. (3.17)], $q_{\rm lin}$ by Eq. (3.20), and $q_{\rm VFP}$ obtained from VFP code; (b) temperature gradient ∇T. The temperature profile is as in Fig. 10, Z=1, and t=10τ_{ei}.

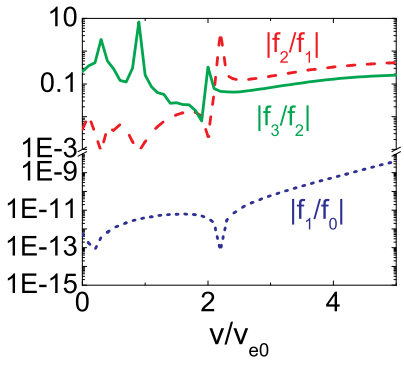

Figure 12: $|f_1/f_0|$, $|f_2/f_1|$ and $|f_3/f_2|$ at $z=z_{\max}/3$ of Fig. 11. f_l is the l-order Legendre expansion coefficient of EDF.

in Table 2. With the response time and the modified heat conductivity, we can calculate the heat flux as

$$q_{\texttt{lin}} = -\gamma_{\text{VFP}}\kappa_L\left[1-\exp(-\frac{t}{\tau_q})\right]\nabla T_e. \tag{3.20}$$

As shown in Fig. 11, the modified linear heat transport model, i.e. Eq. (3.20) with the modified heat conductivity γ_{VFP} instead of Spitzer-Härm's heat conductivity γ_{SH}, can estimate the heat flux accurately at the whole computational region under a small temperature gradient.

The deviation of the Spitzer-Härm heat conductivity from the conductivity obtained from the VFP simulation is induced by the diffusive approximation $|f_l| \ll |f_{l-1}| \cdots |f_2| \ll |f_1| \ll |f_0|$ in the Spitzer-Härm transport theory. As shown in Fig. 12, $|f_3| \ll |f_2|$ and $|f_2| \ll |f_1|$ cannot always be satisfied even under such a weak temperature gradient. Therefore, Spitzer-Härm's model with the diffusive approximation is not competent to accurately calculate the heat conductivity, and it is essential to use the fully $e-e$ collision operator as we have done in our VFP simulations. On the other hand, since $e-i$ collisions become more and more important with the increasing ionic charge state Z, the role of $e-e$ collisions can be negligible for a large value Z. As a result, the deviation of Spitzer-Härm's heat conductivity that induced by the simplified $e-e$ collision operator with diffusive approximation becomes smaller with the increasing Z as shown in Table 2. Finally, both the Spitzer-Härm heat conductivity and the conductivity from the VFP simulation should converge to the Lorentz heat conductivity with the increasing Z, i.e. $\gamma_{\text{SH}}, \gamma_{\text{VFP}} \to 1$ as shown in Table 2.

In order to compare the heat transport under different temperature gradients, we choose the different ΔT as 50 eV, 200 eV and 500 eV in Eq. (3.19) for the temperature profile with the fixed parameters $T_0 = 100$ eV, $z_{\max} = 300$ μm and $Z = 16$. The time evolution of heat flux at $z = z_{\max}/2$ for these different ΔT are drawn in Fig. 13. For $\Delta T = 50$ eV, λ_{ei}/L is only about 6×10^{-4} at $z = z_{\max}/2$, thus the linear perturbation theory should be satisfied. So the heat flux can achieve a steady value, and the steady flux is in a good agreement with the analytically predicted value by Eq. (3.20). For $\Delta T = 200$ eV, λ_{ei}/L is about 5×10^{-3} at $z = z_{\max}/2$, which has slightly exceeded the threshold value 2×10^{-3} for the validity of linear perturbation theory. As a result, the heat flux can not achieve a steady value as large as that predicted by Eq. (3.20). For $\Delta T = 500$ eV, λ_{ei}/L is about 2.5×10^{-2} at $z = z_{\max}/2$, which is far from the validity region of the linear perturbation theory. Therefore, the heat flux is much lower than that predicted by Eq. (3.20) and a very strong "heat inhibition" occurs.

For the steep temperature gradient with $\Delta T = 500$ eV, the spatial profile of the heat flux and temperature is shown in Fig. 14. In this case the heat flux can no longer be determined by the local temperature gradient, so not only the ratio divergence but also the shape divergence are present between the heat flux profile obtained from the VFP simulation and that predicted by the modified linear heat transport model [Eq. (3.20)]. At the middle of heat front $z = z_{\max}/2$, the "heat inhibition" occurs as discussed above. While the heat flux before the heat front (at about $z = 2z_{\max}/3$) obviously exceeds the

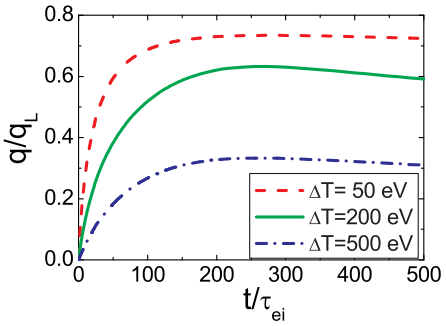

Figure 13: Time evolution of heat flux at $z=z_{\max}/2$ for the temperature profiles as Eq. (3.19) with the fixed $T_0=100$ eV, $z_{\max}=300$ μm and $Z=16$ and the different ΔT as 50 eV, 200 eV and 500 eV. Heat flux is in unit of $q_L=-K_L\nabla T_e$.

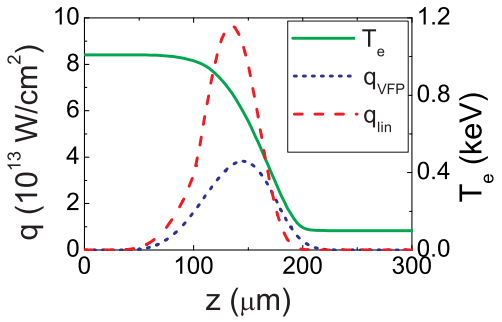

Figure 14: Spatial distributions of the temperature T_e, the heat flux $q_{\mathtt{lin}}$ estimated by Eq. (3.20), and $q_{\mathtt{VFP}}$ obtained from VFP code at $t=320\tau_{ei}$ for the initial temperature profiles as Eq. (3.19) with $\Delta T=500$ eV, $T_0=100$ eV, $Z=16$ and $z_{\max}=300$ μm.

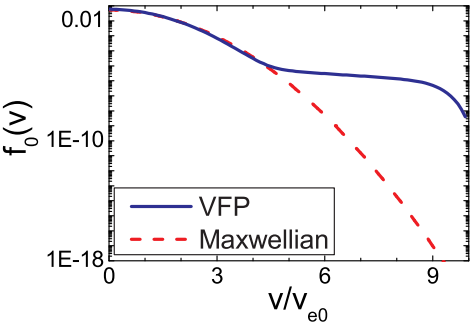

Figure 15: The isotropic part of EDF f_0 at $z=2z_{\max}/3$ of Fig. 14. The Maxwellian distribution with the same temperature is drawn for comparison.

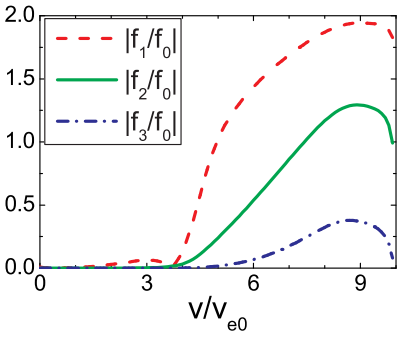

Figure 16: f_1/f_0, f_2/f_0 and f_3/f_0 at $z=2z_{\max}/3$ of Fig. 14. f_l is the l-order Legendre expansion coefficient of the EDF.

theoretically predicted value due to the "preheat". The hydrodynamic codes with the flux limiter can already treat the "heat inhibition" quite well, but they cannot give a description of the "preheat" in the nonlocal heat transport. Thus the "preheat" can be considered as the essential phenomena of the nonlocal heat transport, and it can only be self-consistently described by the kinetic theory or partially by some nonlocal thermal transport models with delocalized convolutions.

As shown in Fig. 15, the relative high energy part of the EDF is much higher than the corresponding Maxwellian distribution due to the "preheat" at the position before the heat front. These relative hot electrons come from the left with a velocity higher than the thermal velocity, so they flow much faster than normal electrons and bring up the "preheat" due to their longer mean free pathes. Meanwhile, the collision frequency at the relative high energy part of the EDF is much low, so this non-Maxwellian high energy part of the EDF can exist for a long time before the heat front. Actually, these hot electrons not only bring up the "preheat", but also result in that the high order Legendre expansion coefficients of the EDF can not be neglected. As shown in Fig. 16, it is found

that the anisotropic part of EDF is comparable with or even bigger than the isotropic part of EDF at the relative high energy part of the EDF. This implies that the diffusive approximation $f_2 \ll f_1 \ll f_0$ is usually failed under the steep temperature gradient, and the attention should be paid to the applicability of the simplified VFP codes that based on the diffusive approximation as well as the Spitzer-Härm transport theory.

In [33], the nonlocal heat transport relevant to the Thomson scattering experiment has been investigated by the experiment observation, Spitzer-Härm's transport theory, and our VFP simulation. It is found that the hydrocode MED103 [42], which is based on the Spitzer-Härm transport theory, must employ an artificial flux limiter to handle the "heat inhibition" near the critical surface. While our VFP simulations can properly treat the nonlocal heat transport in this Thomson scattering experiment.

3.4 Numerical parameters and performance

Numerical parameters, memory usage, and CPU time per 1000 steps for the simulations in Sections 3.1-3.3 have been listed in Table 3. These simulations were done on a personal computer with a 2.8 GHz Intel Core 2 Duo processor, a 2 GB of RAM, and the Microsoft Windows XP Professional operating system. The first five Legendre polynomials were used to calculate the coefficients $\mathbf{D}^{e|e}$, $\mathbf{F}^{e|e}$ of $e-e$ collisions in these simulations, and we found it is enough to generate the results as accurate as those with the first ten Legendre polynomials in all of the above simulations. Since we update $\partial f^e/\partial t = L_{\mathbf{x}} f^e$ in the configuration space by the positive and flux conservative (PFC) method, it is free from the Courant-Friedrichs-Levy (CFL) condition on the time step in contrast to classical Eulerian algorithms [3]. However, in order to follow the detailed time-evolution of the EDFs during the current and the heat flux generation or during one laser cycle, we use a very short time step as $0.01\tau_{ei}$ or $\tau_L/128$ in these simulations. For the simulation box with $z_{\max}$=300 μm that used in Section 3.3, the space step is $z_{\max}/100$=3 μm. While the electron mean free path λ is only about 0.014 μm for $Z=16$ and the basic temperature $T_0=100$ eV, so the bulk of electrons at 100 μm $\leq z \leq$ 200 μm cannot reach the boundary of simulation box in the simulations, and only a few electrons with $v \gg v_{e0}$ may reach the boundary as a byproduct phenomenon of "preheat". Furthermore, our numerical scheme and the

Table 3: Numerical parameters, memory usage, and CPU time per 1000 steps for simulations in Sections 3.1-3.3. τ_L is the laser cycle.

Simulations in	Sec. 3.1	Sec. 3.2	Sec. 3.3
$v_{\max}$	$20v_{e0}$	$20v_{e0}$	$20v_{e0}$
Δv	$0.1v_{e0}$	$0.1v_{e0}$	$0.1v_{e0}$
$\Delta\theta$	$\pi/90$	$\pi/90$	$\pi/90$
Δz	-	-	$z_{\max}/100$
Δt	$0.01\tau_{ei}$	$\tau_L/128$	$0.01\tau_{ei}$
Memory usage	5.14MB	5.81MB	19.02MB
CPU time per 10^3 steps	39.8s	57.8s	4192.3s

reflected boundary combine to make our code satisfies the strict particle number conservation and the good energy conservation. For example, the error of energy is only about 0.064% in the simulation relevant to the Fig. 14.

4 Summary

Based on the positive and flux conservation method and the finite volume method, we have developed a 1D2V VFP simulation code, in which the fully $e-e$ collisions are treated self-consistently. Therefore our code is particularly competent for simulating the highly nonlinear processes with highly non-Maxwellian EDFs in high-power laser/beam-plasma interactions relevant with inertial confinement fusion and the fast ignition of fusion targets.

By our VFP code, the plasma current generation in a DC electric field has been studied systematically with a wide range of field strength. We find that the EDF can be generally expressed as the sum of a stationary and a drifting Maxwellian EDF at any time in a DC electric field. Based on this, a set of hydrodynamic-like equations (3.4)-(3.6) are given for calculating the generated plasma current as well as the parallel and the perpendicular temperatures. It can be used as conveniently as the classical Spitzer-Härm electric transport theory but without the weak-field limit. Furthermore, it is found that the current attenuation after turning off the field is much longer than the current generation in a strong DC electric field. This is due to the significant decrease of the collision frequency for a drifting Maxwellian EDF with a high effective temperature.

We have also simulated the IB absorption and the time evolution of the EDF at a moderate laser intensity. Considering the EDF nearly isotropic in the comoving frame, we have obtained an IB operator for handling the nonlinear IB absorption consistently with a wide range of plasma temperature at the high laser intensity. In particular, our IB operator is suitable to treat the IB absorption accurately with the laser and plasma parameters relevant to shock ignition and impact ignition ICF research with mega-joule level laser energy such as the NIF and LMJ laser facilities.

Using our VFP code, we investigate the heat transport in laser-produced plasmas with different temperature gradients. For a very small temperature gradient, it is confirmed that the heat flux is proportional to the temperature gradient, but a modified heat conductivity instead of the Spitzer-Härm heat conductivity should be used to calculate the heat flux accurately. While the nonlocality of electron heat transport appears under a very steep temperature gradient. In the main body of the heat front the heat flux is significantly smaller than that predicted by Spitzer and Härm, and at the foot of the heat front the heat flux exceeds the theoretically predicted value due to the "preheat" by the hot electrons. Furthermore, simulations show that the assumption of weak anisotropy of the EDF will not be satisfied under a steep temperature gradient. It is thus necessary to use kinetic simulation such as with our VFP code, which contains the fully $e-e$ collision term, to simulate the nonlocal heat transport self-consistently.

Acknowledgments

This work was supported by the National Natural Science Foundation of China (Grants No. 11075105, 10947108) and the National Basic Research Program of China (Grant No. 2009GB105002). One of the authors (S.M.W.) wishes to thank Professor P. Mulser of Technische Universität Darmstadt and Professor M. Murakami of Osaka University for fruitful discussions and suggestions and acknowledges support from the Alexander von Humboldt Foundation. H. Xu acknowledges support from the Natural Science Foundation of Shandong Province (Grand No. Q2008A05). The authors wish to acknowledge Professor P. Norreys, Dr. M. Sherlock, and Dr. A. Robinson from Rutherford Appleton Laboratory for fruitful discussions on some relevant topics discussed in this work, Dr. Q.Z. Yu and Professor Y.T. Li for helpful discussions on nonlocal heat transport in their experiment, and in particular, Academician X.T. He for his encouragement.

The authors are also grateful to three anonymous referees for helpful comments and suggestions on an earlier version of this paper.

References

[1] L. Spitzer and R. Härm, Transport phenomena in a completely ionized gas, Phys. Rev., 89(1953), 977-981.
[2] A. B. Langdon, Nonlinear inverse bremsstrahlung and heated-electron distributions, Phys. Rev. Lett., 44(1980), 575-579.
[3] F. Filbet, E. Sonnendrücker and P. Bertrand, Conservative numerical schemes for the Vlasov equation, J. Comput. Phys., 172(2001), 166-187.
[4] E. Fijalkow, A numerical solution to the Vlasov equation, Comput. Phys. Commun., 116(1999), 319-328.
[5] S. M. Weng, Z. M. Sheng, M. Q. He, H. C. Wu, Q. L. Dong, and J. Zhang, Inverse bremsstrahlung absorption and the evolution of electron distributions accounting for electron-electron collisions, Phys. Plasmas, 13(2006), 113302.
[6] C. F. F. Karney, Fokker-Planck and quasilinear codes, Comput. Phys. Rep., 4(1986), 183-244.
[7] B. A. Trubnikov, Particle imteractions in a fully ionized plasma, Reviews of Plasma Physics, 1(1965), 105-204.
[8] L. Chacón, D. C. Barnes, D. A. Knoll and G. H. Miley, An implicit energy-conservative 2D Fokker-Planck algorithm: I. Difference scheme, J. Comput. Phys., 157(2000), 618-653.
[9] J. S. Chang and G. Cooper, A practical difference scheme for Fokker-Planck equations, J. Comput. Phys., 6(1970), 1-16.
[10] G. I. Marchuk, Methods of numerical mathematics, Springer-Verlag, New York, 1975.
[11] J. F. Benage, W. R. Shanahan, and M. S. Murillo, Electrical resistivity measurements of hot dense aluminum, Phys. Rev. Lett., 83(1999), 2953-2956; D. E. Lencioni, Measurement of plasma conductivity for electric fields larger than the runaway field, Phys. Fluids, 14(1971), 566-569; B. H. Hui, N. K. Winsor, and B. Coppi, Collisional theory of electrical resistivity in trapped electron regimes, Phys. Fluids, 20(1977), 1275-1278.
[12] I. P. Shkarofsky, M. M. Shoucri, and V. Fuchs, Numerical solution of the Fokker-Planck equation with a dc electric field, Comput. Phys. Commun., 71(1992), 269-284.

[13] I. P. Shkarofsky, T. W. Johnston, and M. P. Bachynski, The particle kinetics of plasma, Addison-Wesley, Reading, Mass., 1966
[14] S. M. Weng, Z. M. Sheng, M. Q. He, J. Zhang, P. A. Norreys, M. Sherlock, and A. P. L. Robinson, Plasma currents and electron distribution functions under a dc electric field of arbitrary strength, Phys. Rev. Lett., 100(2008), 185001.
[15] H. Dreicer, Electron and ion runaway in a fully ionized gas. I, Phys. Rev., 115(1959), 238-249; H. Dreicer, Electron and ion runaway in a fully ionized gas. II, Phys. Rev., 115(1960), 329-342.
[16] R. J. Goldston and P. H. Rutherford, Introduction to plasma physics, Institute of Physics Publishing, Bristol, 1995.
[17] J. Meyer-ter-Vehn et al., On electron transport in fast ignition research and the use of few-cycle PW-range laser pulses, Plasma Phys. Controlled Fusion, 47(2005), B807-B813.
[18] J. J. Honrubia and J. Meyer-ter-Vehn, Three-dimensional fast electron transport for ignition-scale inertial fusion capsules, Nucl. Fusion, 46(2006), L25-L28.
[19] G. J. Pert, Inverse bremsstrahlung in strong radiation fields at low temperatures, Phys. Rev. E, 51(1995), 4778-4789.
[20] R. Betti, C.D. Zhou, K. S. Anderson *et al.*, Shock ignition of thermonuclear fuel with high areal density, Phys. Rev. Lett., 98(2007), 155001; L. J. Perkins, R. Betti, K. N. LaFortune, and W. H. Williams, Shock ignition: a new approach to high gain inertial confinement fusion on the national ignition facility, Phys. Rev. Lett., 103(2009), 045004; X Ribeyre, G Schurtz, M Lafon, S Galera and S Weber, Shock ignition: an alternative scheme for HiPER, Plasma Phys. Control. Fusion, 51(2009), 015013.
[21] M. Murakami and H. Nagatomo, A new twist for inertial fusion energy: Impact ignition, Nucl. Inst. and Meth. in Phys. Res. A, 544(2005), 67; M. Murakami, H. Nagatomo, H. Azechi, F. Ogando, and S. Eliezer, Innovative ignition scheme for ICF-impact fast ignition, Nucl. Fusion, 46(2006), 99; M. Karasik, J. L. Weaver, Y. Aglitskiy *et al.*, Acceleration to high velocities and heating by impact using Nike KrF laser, Phys. Plasmas, 17(2010), 056317.
[22] Y. Ping, R. Shepherd, B. F. Lasinski *et al.*, Absorption of short laser pulses on solid targets in the ultrarelativistic regime, Phys. Rev. Lett., 100(2008), 085004.
[23] P. Gibbon, Short pulse laser interactions with matter, Imperial College Press, London, 2005.
[24] S. C. Wilks and W. L. Kruer, Absorption of ultrashort, ultra-intense laser light by solids and overdense plasmas, IEEE J. Quantum Electron., 33(1997), 1954.
[25] D. F. Price, R.M. More, R. S.Walling *et al.*, Absorption of ultrashort laser pulses by solid targets heated rapidly to temperatures 1ł1000 eV, Phys. Rev. Lett., 75(1995), 252.
[26] C. P. Ridgers, R. J. Kingham, and A. G. R. Thomas, Magnetic cavitation and the reemergence of nonlocal transport in laser plasmas, Phys. Rev. Lett., 100(2008), 075003.
[27] S. M. Weng, Z. M. Sheng, and J. Zhang, Inverse bremsstrahlung absorption with nonlinear effects of high laser intensity and non-Maxwellian distribution, Phys. Rev. E, 80(2009), 056406.
[28] P. Mulser, F. Cornolti, E. Bésuelle, and R. Schneider, Time-dependent electron-ion collision frequency at arbitrary laser intensity-temperature ratio, Phys. Rev. E, 63(2000), 016406.
[29] E. Bésuelle, R. R. E. Salomaa, and D. Teychenné, Coulomb logarithm in femtosecond-laser-matter interaction, Phys. Rev. E, 60(1999), 2260-2263.
[30] N. David, D. J. Spence, and S. M. Hooker, Molecular-dynamic calculation of the inverse-bremsstrahlung heating of non-weakly-coupled plasmas, Phys. Rev. E, 70(2004), 056411.
[31] A. R. Bell and R. J. Kingham, Resistive collimation of electron beams in laser-produced plasmas, Phys. Rev. Lett., 91(2003), 035003; and reference therein.
[32] A. R. Bell, Electron energy transport in ion waves and its relevance to laser-produced plas-

mas, Phys. Fluids, 26(1983), 279-284.
[33] Q. Z. Yu, Y. T. Li, S. M. Weng, Q. L. Dong, F. Liu, Z. Zhang, J. Zhao, X. Lu, C. Danson, D. Pepler, X. H. Jiang, Y. G. Liu, L. Z. Huang, S. Y. Liu, Y. K. Ding, Z. B. Wang, Y. Gu, X. T. He, Z. M. Sheng, and J. Zhang, Nonlocal heat transport in laser-produced aluminum plasmas, Phys. Plasmas, 17(2010), 043106.
[34] R. Fabbro, C. Max and E. Fabre, Planar laser-driven ablation: Effect of inhibited electron thermal conduction, Phys. Fluids, 28(1985), 1463-1481.
[35] J. Hawreliak, D. M. Chambers, S. H. Glenzer, A. Gouveia, R. J. Kingham, R. S. Marjoribanks, P. A. Pinto, O. Renner, P. Soundhauss, S. Topping, E. Wolfrum, P. E. Young, and J. S. Wark, Thomson scattering measurements of heat flow in a laser-produced plasma, J. Phys. B, 37(2004), 1541-1551.
[36] R. C. Malone, R. L. McCrory and R. L. Morse, Indications of strongly flux-limited electron thermal conduction in laser-target experiments, Phys. Rev. Lett., 34(1975), 721-724.
[37] A. R. Bell, R. Evans and D. J. Nicholas, Elecron energy transport in steep temperature gradients in laser-produced plasmas, Phys. Rev. Lett., 46(1981), 243-246.
[38] J. F. Luciani and P. Mora, Nonlocal heat transport due to steep temperature gradients, Phys. Rev. Lett., 51(1983), 1664-1667; G. P. Schurtz, Ph. D. Nicola ï, and M. Busquet, A nonlocal electron conduction model for multidimensional radiation hydrodynamics codes, Phys. Plasmas, 7(2000), 4238.
[39] J. R. Albritton, E. A. Williams, and I. B. Bernstein, Nonlocal electron heat transport by not quite Maxwell-Boltzmann distributions, Phys. Rev. Lett., 57(1986), 1887-1890.
[40] Y. Kishimoto, K. Mima, and M. G. Haines, An extension of Spitzer-Härm theory on thermal transport to steep temperature gradient case. II. Integral representation, J. Phys. Soc. Jpn., 57(1988), 1972-1986.
[41] V. N. Goncharov, O. V. Gotchev, and E. Vianello, Early stage of implosion in inertial confinement fusion: Shock timing and perturbation evolution, Phys. Plasmas, 13(2006), 012702.
[42] J. P. Christiansen, D. E. T. F. Ashby and K. V. Roberts, MEDUSA a one-dimensional laser fusion code, Comput. Phys. Commun., 7(1974), 271-287.